Applied Mathematical Modelling 39 (2015) 531–547

Contents lists available at ScienceDirect

Applied Mathematical Modelling

journal homepage: www.elsevier.com/locate/apm

Mathematical model of electrical and mechanical yielding for piezoelectric strip weakened by a non-centric semi-permeable crack

R.R. Bhargava, Pooja Raj Verma *

Department of Mathematics, Indian Institute of Technology Roorkee, Roorkee 247667, India

ARTICLE INFO

Article history:
Received 9 May 2013
Received in revised form 28 February 2014
Accepted 12 June 2014
Available online 21 June 2014

Keywords:
Crack opening potential drop
Crack sliding displacement
Energy release rate
Field intensity factors
Fourier integral transform
Semi-permeable crack

ABSTRACT

A mathematical strip-electro-elastic yielding model solution is obtained for a long and narrow piezoelectric strip weakened by a non-centric, semi-permeable, mode-III crack. The crack is oriented parallel and situated asymmetrically with respect to the edges of the strip. Fourier cosine integral transform technique is adopted to solve the problem. Three different cases are considered: when developed saturation zone is bigger, smaller or equal to the developed slide-yield zone. Closed-form analytic expressions are derived for developed zones lengths, crack sliding displacement, crack opening potential drop, field intensity factors and energy release rate. A numerical case study is presented for poled $BaTiO_3$ piezoelectric ceramic which affirms that proposed model is capable of crack arrest under small-scale mechanical and electrical yielding.

1. Introduction

The proven vast utility of piezoelectric ceramics as sensor/actuator/transducers in high-tech equipment have drawn the attention of researchers to understand the crack behavior and mechanics of fracture of such materials. A lot of work has been done on fracture analysis of piezoelectric material since nineties.

The present paper deals with semi-permeable crack-face boundary condition [1], mathematically, represented as:

$$D_n^+ = D_n^-, \quad D_n^+(\phi^+ - \phi^-) = -\varepsilon_0(w^+ - w^-),$$

where D_n, ϕ and w, ε_0 denote electric displacement component, potential and displacement, electric permitivity of crack media. The superscripts +, − denote the value of the quantity on upper and lower crack rims, respectively.

Using non-local theory, the behavior of a mode-I crack subjected to a uniform tension loading in piezoelectric materials is investigated in [2]. The influence of different crack-face boundary conditions on crack energy density for piezoelectric material is studied in [3]. The semi-permeable crack problem in a non-local piezoelectric materials is solved in [4] using Newton iterative method. The effects of crack size and electric permeability of the crack on electromechanical properties of the piezoelectric materials are obtained in [5].

A lot of work has been reported on crack problems but very few work on crack arrest problem for piezoelectric materials using various suitable techniques has been reported. A strip-saturation zone model [6] for impermeable crack in an infinite

* Corresponding author. Tel.: +91 8909486368.
E-mail addresses: rajrbfma@iitr.ac.in (R.R. Bhargava), poojarajvs@gmail.com (P.R. Verma).

http://dx.doi.org/10.1016/j.apm.2014.06.007
0307-904X/

piezoelectric ceramic plate was proposed under the assumption of Dugdale model [7]. They [6] also calculated local and global energy release rates for strip-saturation for piezoelectric ceramics plate. A strip-electric saturation model for an impermeable crack weakening a piezoelectric material was studied in [8]. The strip-saturation model for piezoelectric ceramic was further re-examined in [9].

Strip-yield models [10,11] were proposed for longitudinal and transverse crack in an orthotropic piezoelectric strip under mode-III deformation. A strip-electrical and mechanical yielding model was developed [12] for a mode III interfacial crack with electrical polarization reaching a saturation limit and shear stress reaching a yield stress along a line segment in front of the crack. Their work was further extended [13] to crack problem in piezoelectric strip.

A strip-saturation model based on Dugdale-type assumption for electric displacement was proposed to evaluate the electric field induced stress intensity factor in a piezoelectric medium of limited electrical polarization in [14]. An electrically dielectric Griffith crack in a piezoelectric layer under in-plane electro-mechanical loads and semi-permeable boundary conditions was proposed in [15]. A strip-yield and saturation model for limited permeable crack situated in a thin interlayer between two identical piezoelectric materials was analyzed in [16] using Stroh formalism and complex variable technique.

In present paper, for the first time a strip-electroelastic yield model under mode-III condition for a non-centric semi-permeable crack in an infinitely long and narrow piezoelectric strip is proposed. The present paper is organized as follows: In Section 2, fundamental formulation of the problem is presented; statement of the problem and mathematical model are given in Sections 3 and 4, respectively; closed-form analytic expressions for crack sliding displacement (CSD), crack opening potential drop (COP), field intensity factors (IFs) and energy release rate (ERR) and illustrative case study for $BaTiO_3$ cracked strip for three cases when saturation zone is bigger, smaller or equal to developed slide-yield zone are derived in Sections 5, 6 and 7, respectively; The last Section 8 gives conclusions of the problem.

2. Fundamental formulation

As are well-known, out-of-plane displacement and in-plane electric field problems may be written as

$$u_x(x,y,z)=0,\quad u_y(x,y,z)=0\ \text{ and }\ u_z(x,y,z)=w(x,y), \tag{1}$$

$$E_x(x,y,z)=E_x(x,y),\quad E_y(x,y,z)=E_y(x,y)\ \text{ and }\ E_z(x,y,z)=0. \tag{2}$$

Out-of-plane strain component, $\gamma_{zi}(i=x,y)$, and electric field, E_i, in term of displacement and electric potential, ϕ, may be expressed as

$$\gamma_{zi}=w_{,i}, \tag{3}$$

$$E_i=-\phi_{,i}, \tag{4}$$

respectively, where comma in subscript denotes the partial differentiation with respect to argument following it.

The constitutive relations for stress component, σ_{zi}, and electric displacement, D_i $(i=x,y)$, may be written as

$$\sigma_{zi}=c_{44}w_{,i}+e_{15}\phi_{,i}; \tag{5}$$

$$D_i=e_{15}w_{,i}-\varepsilon_{11}\phi_{,i}, \tag{6}$$

where c_{44}, e_{15} and ε_{11} denote elastic, piezoelectric and dielectric constants, respectively.

The governing equations for piezoelectric material under anti-plane deformation and in-plane electric loading are

$$c_{44}\nabla^2 w+e_{15}\nabla^2\phi=0, \tag{7}$$

$$e_{15}\nabla^2 w-\epsilon_{11}\nabla^2\phi=0, \tag{8}$$

where $\nabla^2=\frac{\partial^2}{\partial x^2}+\frac{\partial^2}{\partial y^2}$, is two-dimensional Laplacian operator.

3. Statement of the problem

An infinitely long transversely isotropic piezoelectric strip occupies the region $-h_2\leqslant y\leqslant h_1$ (h_1 may not be equal to h_2) and $|x|<\infty$ in xoy-plane and is thick enough in z-direction to allow anti-plane deformations. The strip is poled along z-direction and weakened by a mechanically stress free and electrically semi-permeable straight hairline crack, cut along $[-a,a]$ on x-axis. The crack is oriented parallel to the edges of the strip and situated off center line of the strip. The boundaries of the piezoelectric strip are prescribed uniform constant anti-plane mechanical shear stress, $\sigma_{zy}=\tau_0$, and in-plane electric displacement, $D_y=D_0$. Consequently, crack opens in self-similar fashion forming a slide-yield and a saturation zones ahead each tip of the crack. These developed slide-yield and saturation zones occupy the intervals $[-b,-a]$, $[a,b]$ and $[-c,-a]$, $[a,c]$ on x-axis, respectively. To stop the crack from further opening, the rims of developed slide-yield zone are prescribed cohesive yield point anti-plane shear stress, $\sigma_{zy}=\tau_s$, and rims of developed saturation zone are subjected to in-plane normal cohesive polarization limit of electric-displacement, $D_y=D_s$. Three cases considered are: when

Case I. Saturation zone is bigger than slide-yield zone ($c > b$),
Case II. Saturation zone is smaller than slide-yield zone ($c < b$),
Case III. Saturation zones and slide-yield zones are of equal length ($c = b$).
Schematic configuration of the problem is depicted in Fig. 1.

4. Mathematical model

Mathematically, the physical boundary conditions of the problem may be expressed as
(i) on the strip edges $y = h_1$ and $y = -h_2$

$$\sigma_{zy(1)}(x, h_1) = \sigma_{zy(2)}(x, -h_2) = \tau_0, \quad D_{y(1)}(x, h_1) = D_{y(2)}(x, -h_2) = D_0,$$

where subscript (1) refers to piezoelectric material layer for upper region $0 < y < h_1$ and subscript (2) refers to material in lower region $-h_2 < y < 0$ of the strip.
(ii) boundary conditions on the developed slide- yield and saturation zones are

(a) $\sigma_{zy(1)}(x, 0^+) = \sigma_{zy(2)}(x, 0^-) = \tau_s, \quad a < |x| < b,$
(b) $D_{y(1)}(x, 0^+) = D_{y(2)}(x, 0^-) = D_s, \quad a < |x| < c,$

(iii) by principle of superposition, electro-elastic boundary conditions over the crack surfaces including rims of developed zones along the line $y = 0$, may be written as

(a) $\sigma_{zy(1)}(x, 0^+) = \sigma_{zy(2)}(x, 0^-) = -\tau_0 + H(x-a)\tau_s, \quad 0 < x < b,$
(b) $D_{y(1)}(x, 0^+) = D_{y(2)}(x, 0^-) = -D_0(1 - D_r) + H(x-a)D_s, \quad 0 < x < c,$

where D_r is electric crack condition parameter (ECCP), introduced in [17]. D_r is zero for impermeable condition case, $(D_r)_{\text{perm}}$ for permeable condition case to be determined for each Cases I, II and III in Sections 5, 6, and 7 and for semi-permeable crack, $0 < D_r < (D_r)_{perm}$. $H(\cdot)$ denotes Heaviside function.
(iv) electro-elastic continuity conditions along the line $y = 0$ are defined as

(a) $w_{(1)}(x, 0^+) = w_{(2)}(x, 0^-), \quad \sigma_{zy(1)}(x, 0^+) = \sigma_{zy(2)}(x, 0^-)$ for $|x| \geqslant b,$
(b) $\phi_{(1)}(x, 0^+) = \phi_{(2)}(x, 0^-), \quad D_{y(1)}(x, 0^+) = D_{y(2)}(x, 0^-)$ for $|x| \geqslant c.$

Governing Eqs. (7) and (8) are solved under above boundary conditions.
Since the problem is symmetric, it is sufficient to consider for region $0 \leqslant x < \infty$.

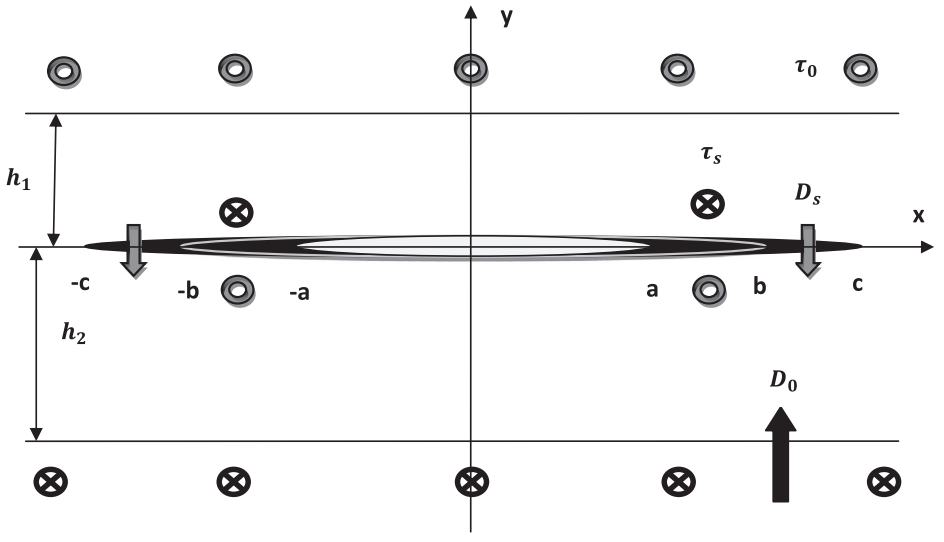

Fig. 1. Schematic representation of the problem.

5. Case I: when saturation zone is bigger than slide-yield zone (c > b)

To simplify the mathematical computational, a new potential function, $\Psi^I(x,y)$, is introduced as

$$\Psi^I(x,y) = \phi^I(x,y) - (e_{15}/\epsilon_{11})w^I(x,y), \tag{9}$$

where superscript I is refer to Case I.

This potential function reduces Eqs. (3)–(8) to

$$\sigma^I_{zy} = \bar{c}_{44}\gamma^I_{zy} + e_{15}\Psi^I_{,y}, \tag{10}$$

$$D^I_y = -\epsilon_{11}\Psi^I_{,y}, \tag{11}$$

$$\gamma^I_{zy} = w^I_{,y}, \tag{12}$$

$$E^I_y = -\Psi^I_{,y} - (e_{15}/\epsilon_{11})w^I_{,y}, \tag{13}$$

$$\nabla^2 w^I = 0 \text{ and } \nabla^2\Psi^I = 0, \tag{14}$$

$$\text{where } \bar{c}_{44} = c_{44} + (e^2_{15}/\epsilon_{11}). \tag{15}$$

The solutions of Eq. (14) is written using Fourier cosine integral transform as

$$w^I_{(i)}(x,y) = \int_0^\infty \left[A_{(i)}(\xi)\cosh(y\xi) + B_{(i)}(\xi)\sinh(y\xi)\right]\cos(x\xi)d\xi, \tag{16}$$

$$\Psi^I_{(i)}(x,y) = \int_0^\infty \left[C_{(i)}(\xi)\cosh(y\xi) + F_{(i)}(\xi)\sinh(y\xi)\right]\cos(x\xi)d\xi, \tag{17}$$

where $A_{(i)}(\xi)$, $B_{(i)}(\xi)$, $C_{(i)}(\xi)$ and $F_{(i)}(\xi)$ $(i = 1,2)$ are arbitrary functions and to be determined using boundary conditions of the problem.

Expressions for stress, electric-displacement, strain and electric field are obtained using Eqs. (10)–(13) substituting from Eqs. (16) and (17) as

$$\sigma^I_{zy(i)}(x,y) = \int_0^\infty \xi\left[\left\{\bar{c}_{44}A_{(i)}(\xi) + e_{15}C_{(i)}(\xi)\right\}\sinh(y\xi) + \left\{\bar{c}_{44}B_{(i)}(\xi) + e_{15}F_{(i)}(\xi)\right\}\cosh(y\xi)\right]\cos(x\xi)d\xi, \tag{18}$$

$$D^I_{y(i)}(x,y) = -\epsilon_{11}\int_0^\infty \xi\left[C_{(i)}(\xi)\sinh(y\xi) + F_{(i)}(\xi)\cosh(y\xi)\right]\cos(x\xi)d\xi, \tag{19}$$

$$\gamma^I_{zy(i)}(x,y) = \int_0^\infty \xi\left[A_{(i)}(\xi)\sinh(y\xi) + B_{(i)}(\xi)\cosh(y\xi)\right]\cos(x\xi)d\xi, \tag{20}$$

$$E^I_{y(i)}(x,y) = -\int_0^\infty \xi\left[\left\{(e_{15}/\epsilon_{11})A_{(i)}(\xi) + C_{(i)}(\xi)\right\}\sinh(y\xi) + \left\{(e_{15}/\epsilon_{11})B_{(i)}(\xi) + F_{(i)}(\xi)\right\}\cosh(y\xi)\right]\cos(x\xi)d\xi. \tag{21}$$

Applying boundary conditions (i) and (iv) in Eqs. (18) and (19), one obtains relations amongst arbitrary functions as

$$B_{(1)}(\xi) = -A_{(1)}(\xi)\tanh(h_1\xi), \quad F_{(1)}(\xi) = -C_{(1)}(\xi)\tanh(h_1\xi), \tag{22}$$

$$B_{(2)}(\xi) = A_{(2)}(\xi)\tanh(h_2\xi), \quad F_{(2)}(\xi) = C_{(2)}(\xi)\tanh(h_2\xi), \tag{23}$$

$$B_{(1)}(\xi) = B_{(2)}(\xi) \text{ and } F_{(1)}(\xi) = F_{(2)}(\xi). \tag{24}$$

Simplifying Eqs. (22)–(24), one obtains

$$A_{(2)}(\xi) = -A_{(1)}(\xi)M_{12}(\xi) \text{ and } C_{(2)}(\xi) = -C_{(1)}(\xi)M_{12}(\xi), \tag{25}$$

where $M_{12}(\xi) = \tanh(h_1\xi)\coth(h_2\xi)$.

Using Eqs. (16)–(19) and electro-elastic boundary conditions (iii) and (iv), two set of dual integral equations are obtained as

$$\epsilon_{11}\int_0^\infty \xi C_{(1)}(\xi)\tanh(h_1\xi)\cos(x\xi)d\xi = -f_1 + D_s H(x-a), \quad 0 \leqslant x < c, \tag{26}$$

$$\int_0^\infty [1 + M_{12}(\xi)]\{\epsilon_{11}C_{(1)}(\xi) + e_{15}A_{(1)}(\xi)\}\cos(x\xi)d\xi = 0, \quad c \leqslant x < \infty, \tag{27}$$

where $f_1 = D_0(1 - D_r)$, (28)

and

$$\int_0^\infty \xi\left[\bar{c}_{44}A_{(1)}(\xi) + e_{15}C_{(1)}(\xi)\right]\tanh(h_1\xi)\cos(x\xi)d\xi = \tau_0 - \tau_s H(x-a), \quad 0 \leqslant x < b, \tag{29}$$

$$\int_0^\infty [1 + M_{12}(\xi)]A_{(1)}(\xi)\cos(x\xi)d\xi = 0, \quad b \leqslant x < \infty. \tag{30}$$

To solve the Eqs. (26) and (27) we introduce

$$C_{(1)}(\xi) = -\frac{2c^2}{[1 + M_{12}(\xi)]}\int_{u=0}^{1}\sqrt{u}\,\Omega_2^I(u)J_0(cu\xi)du, \tag{31}$$

$$A_{(1)}(\xi) = \frac{2b^2}{[1 + M_{12}(\xi)]}\int_{u=0}^{1}\sqrt{u}\,\Omega_1^I(u)J_0(bu\xi)du, \tag{32}$$

where $J_0(\cdot)$ denotes zeroth order Bessel function of first kind.

Consequently by Eq. (31), Eq. (27) is identically satisfied and Eq. (26) leads to

$$\frac{d}{dx}\int_{\xi=0}^{\infty} c^2\left[\int_{u=0}^{1}\sqrt{u}J_0(cu\xi)\Omega_2^I(u)du\right]\sin(x\xi)d\xi = p(x), \tag{33}$$

where

$$p(x) = \frac{-f_1 + D_s H(x-a)}{\epsilon_{11}} - \int_0^\infty \xi\frac{[1 + M_{12}(\xi)]}{2}C_1(\xi)[\chi(\xi) - 1]\cos(x\xi)d\xi, \tag{34}$$

changing of order of integration and using Ryzhik an Gradshteyn {[18] (6,671(8))}

$$\frac{d}{dx}\int_{u=0}^{x}\frac{\sqrt{u}\,\Omega_2^I(u)du}{\sqrt{x^2 - u^2}} = p(cx). \tag{35}$$

The solution of Eq. (35) standardly written as

$$\Omega_2^I(x) = \frac{2}{\pi}\sqrt{x}\int_{u=0}^{x}\left[\frac{-f_1 + D_s H(bu-a)}{\epsilon_{11}} - \int_0^\infty \xi\frac{[1 + M_{12}(\xi)]}{2}C_1(\xi)[\chi(\xi) - 1]\cos(bu\xi)d\xi\right]\frac{du}{\sqrt{x^2 - u^2}}, \tag{36}$$

which on evaluation of right hand side integrals leads to

$$\Omega_2^I(x) + \int_{t=0}^{1}K_2(x,t)\Omega_2^I(t)dt = \frac{\sqrt{x}}{\epsilon_{11}}\left[f_1 - \frac{2}{\pi}D_s\cos^{-1}\frac{a}{cx}\right], \tag{37}$$

where kernel $K_2(x,t)$ is

$$K_2(x,t) = \sqrt{xt}\int_{y=0}^{\infty} y\{\chi(y/c) - 1\}J_0(xy)J_0(ty)dy. \tag{38}$$

Analogously, $\Omega_1^I(.)$ is obtained from the Eqs. (29) and (30) as

$$\Omega_1^I(x) + \int_{t=0}^{1}K_1(x,t)\Omega_1^I(t)dt = \frac{\sqrt{x}}{\bar{c}_{44}\epsilon_{11}}\left[f_2 - \frac{2}{\pi}f_3\cos^{-1}\frac{a}{bx}\right], \tag{39}$$

where $f_2 = \epsilon_{11}\tau_0 + e_{15}f_1$, $f_3 = \epsilon_{11}\tau_s + e_{15}D_s$, and $K_1(x,t)$ kernel is defined as

$$K_1(x,t) = \sqrt{xt}\int_{y=0}^{\infty} y\{\chi(y/b) - 1\}J_0(xy)J_0(ty)dy, \tag{40}$$

with $\chi(y) = 2\tanh(h_1 y)/\{1 + M_{12}(y)\}$.

5.1. Applications

In this section expressions are derived for slide-yield zone length, saturation zone length, IFs, CSD, COP and ERR.

5.1.1. Field intensity factors

Mode-III stress intensity factor, K_{III}^{τ}, and strain intensity factor, K_{III}^{γ}, at $x = b$ are determined as

$$K_{III}^{\tau} = \lim_{x\to b^+}\left\{\sqrt{2\pi(x-b)}\sigma_{zy(1)}^I(x,0^+)\right\} = \bar{c}_{44}\sqrt{\pi b}\,\Omega_1^I(1), \tag{41}$$

$$K_{III}^{\gamma} = \lim_{x\to b^+}\left\{\sqrt{2\pi(x-b)}\gamma^I_{zy(1)}(x,0^+)\right\} = \sqrt{\pi b}\,\Omega_1^I(1). \tag{42}$$

Similarly, mode-I electric-displacement intensity factor, K_I^D, and electric-field intensity factor, K_I^E, $x = c$ are obtained as

$$K_I^D = \lim_{x\to c^+}\left\{\sqrt{2\pi(x-c)}D^I_{y(1)}(x,0^+)\right\} = \epsilon_{11}\sqrt{\pi c}\,\Omega_2^I(1), \tag{43}$$

$$K_I^E = \lim_{x\to c^+}\left\{\sqrt{2\pi(x-c)}E^I_{y(1)}(x,0^+)\right\} = \sqrt{\pi c}\,\Omega_2^I(1). \tag{44}$$

5.1.2. Size of slide-yield zone and saturation zone

Slide-yield zone length is determined assuming Dugdale's [7] hypothesis for stress to remain finite at every point of the strip. Consequently, at the slide-yield zone tip, $x = b$, Eq. (41) together with Eq. (39) yields following equation to determine b

$$\frac{b}{a} = \sec\left(\frac{\pi}{2}.\frac{f_2 - \epsilon_{11}\bar{c}_{44}R_1}{f_3}\right), \tag{45}$$

where $R_1 = \int_{t=0}^{1} K_1(1,t)\,\Omega_1^I(t)dt$ and

$$K_1(1,t) = \sqrt{t}\int_{y=0}^{\infty} y\{\chi(y/b) - 1\}J_0(y)J_0(ty)dy. \tag{46}$$

The slide-yield zone length is then obtained from $|b - a|$.

Analogously, assuming Dugdale hypothesis [7] to be true for electric-displacement to remain finite everywhere in the strip, at the tip $x = c$, a transcendental equation is obtained to determine c using Eqs. (37) and (43) as

$$\frac{c}{a} = \sec\left(\frac{\pi}{2}.\frac{f_1 - \epsilon_{11}R_2}{D_s}\right), \tag{47}$$

where $R_2 = \int_{t=0}^{1} K_2(1,t)\Omega_2^I(t)dt$ and

$$K_2(1,t) = \sqrt{t}\int_{y=0}^{\infty} y\{\chi(y/c) - 1\}J_0(y)J_0(ty)dy.$$

The saturation zone length is obtained using $|c - a|$.

5.1.3. Crack sliding displacement (CSD) and crack opening potential drop (COP)

Relative crack sliding displacement of crack-faces is obtained using

$$\text{CSD} = \Delta w^I(x) = w^I_{(1)}(x,0^+) - w^I_{(2)}(x,0^-). \tag{48}$$

Finding $w^I_{(1)}(x,0^+)$ and $w^I_{(2)}(x,0^-)$ using Eqs. (16) and (39) and substituting in Eq. (48), one obtains

$$\Delta w^I(x) = 2\sqrt{b^2 - x^2}\,\Omega_1^I(1), \quad a \leqslant x < b. \tag{49}$$

Crack opening potential drop (COP) across the developed saturation zone rims is obtained using

$$\text{COP} = \Delta\phi^I(x) = \phi^I_{(1)}(x,0^+) - \phi^I_{(2)}(x,0^-). \tag{50}$$

Using Eqs. (9), (16), (17), (31), (32), (37), and (49) together with Eq. (50) and simplifying, one obtains

$$\Delta\phi^I(x) = 2\sqrt{c^2 - x^2}\Omega_2^I(1) - (e_{15}/\epsilon_{11})\Delta w^I(x), \quad a \leqslant x < c. \tag{51}$$

5.1.4. Determination of ECCP (D_r)

Permeability condition across the crack surfaces yields a equation to determine D_r

$$(D_r)_{\text{perm}} = 1 - \left[\frac{\sqrt{c^2 - x^2}\bar{c}_{44}\left(\frac{2}{\pi}D_s\cos^{-1}\left(\frac{a}{c}\right) - \epsilon_{11}R_3\right) + \sqrt{b^2 - x^2}\left(\epsilon_{11}f_3 - \frac{2}{\pi}f_4\cos^{-1}\left(\frac{a}{b}\right) - \epsilon_{11}\bar{c}_{44}R_2\right)}{D_0\left(\sqrt{c^2 - x^2}\bar{c}_{44} - e_{15}\sqrt{b^2 - x^2}\right)}\right]. \tag{52}$$

Note that when the size of saturation zone and slide-yield zone is very small, $(D_r)_{\text{perm}} \approx 1$ and for the semi-permeable crack, $0 < D_r < (D_r)_{\text{perm}}$.

5.1.5. Energy release rate (ERR)

Energy release rate at crack tip, $x = a$, is obtained using

$$G_a^I = \tau_s\Delta w^I(a) + D_s\Delta\phi^I(a), \tag{53}$$

for Case I. Substituting CSD and COP from Eqs. (49) and (51) into Eq. (53), one obtains

$$G_a^I = 2\{\tau_s - (e_{15}/\epsilon_{11})D_s\}\sqrt{b^2 - a^2}\,\Omega_1^I(1) + 2D_s\sqrt{c^2 - a^2}\,\Omega_2^I(1). \tag{54}$$

5.2. Illustrative case study for Case I

In this section, a qualitative study is presented for $BaTiO_3$ piezoelectric ceramic and material constants of $BaTiO_3$ piezoelectric ceramic are given in Table 1 taken from [19].

Length of crack, prescribed electric displacement and mechanical load are taken as 10 mm, 0.02 C/m^2 and 40 MPa, respectively.

Variation of electrical loading on COP over saturation zone is shown in Fig. 2. It is observed that COP increases as electric displacement is increased from 0.01 to 0.02 C/m^2. In this figure, a kink point on each of three graphs for applied electric loading is observed. This kink point is the tip of slide-yield zone and indicates that up to this kink developed saturation zone is effected both by electrical and mechanical loadings and beyond this point, only electric field effects the saturation zone.

ERR at the crack tip versus prescribed D_0 for various values of prescribed mechanical load ($\tau_0 = 30$, 35 and 40 MPa) is plotted in Fig. 3. The results show that ERR decreases linearly as D_0 is increased. It indicates that electric displacement always retards the crack growth. It is also pointed out that as prescribed mechanical load is increased, the value of ERR increases too but the decreasing trend continues as D_0 increases.

The effect of h_1/a on ERR for centric (when $h_1 = h_2$) and non-centric (when $h_1 \neq h_2$) crack in a piezoelectric strip is drawn in Fig. 4. This figure discloses the important fact that the effect of applied loads on the crack reduces as upper edge (or lower edge) of piezoelectric strip is moved away from the crack. Consequently, energy release rate decreases. It is also observed that ERR is maximum for centric crack as compare to eccentrically located crack for smaller value of $h_1/a < 3$.

Fig. 5 show the variation of ERR versus ECCP (D_r) for three different electric displacement. It may be noted that as the permittivity of the crack gap is increased, the ERR drops, as expected. This indicates that ECCP resists the crack growth.

The influence of crack-face boundary conditions on CSD over slide-yield zone is plotted in Fig. 6. From the figure, it is observed that as we move toward the tip of slide-yield zone, CSD decreases parabolically and becomes zero at $x = b$, as expected. Apart from this, it is also observed that CSD is maximum for impermeable and minimum for permeable crack-face conditions, whereas in case of semi-permeable crack-face boundary condition, CSD lies in between impermeable and permeable crack cases. Which implies that the electric field between the crack gaps cannot be ignored. This is observed experimentally also.

5.3. Validation of obtained results for Case I

Results are validated with Shen et al. [12] when in our results $D_r = 0$, $b < c$, $h_1 \to \infty$ and $h_2 \to \infty$ is substituted in Eqs. (45) and (47), which reduces to the following form of [12]

$$\frac{b}{a} = \sec\left(\frac{\pi}{2}\cdot\frac{\epsilon_{11}\tau_0 + e_{15}D_0}{\epsilon_{11}\tau_s + e_{15}D_s}\right), \tag{55}$$

$$\frac{c}{a} = \sec\left(\frac{\pi}{2}\cdot\frac{D_0}{D_s}\right). \tag{56}$$

6. Case II: when saturation zone is shorter than slide-yield zone ($c < b$)

For this case, the new potential function $\Psi^{II}(x,y)$ is defined as

$$\Psi^{II}(x,y) = w^{II}(x,y) + (e_{15}/c_{44})\phi^{II}(x,y), \tag{57}$$

where superscript II denotes that the quantities refer to Case II.

Similar to Case I, substituting Eq. (57) into Eqs. (3)–(8), the constitutive equations, gradient equations transform to

$$\sigma_{zy}^{II} = c_{44}\Psi_{,y}^{II}, \tag{58}$$

$$D_y^{II} = e_{15}\Psi_{,y}^{II} - \bar{\epsilon}_{11}\phi_{,y}^{II}, \tag{59}$$

Table 1
The material constants of piezoelectric material.

Materials	C_{44} (10^{10} N/m^2)	e_{15} (C/m^2)	ϵ_{11} (10^{-10} C/Vm)
$BaTiO_3$	4.4	11.4	98.7

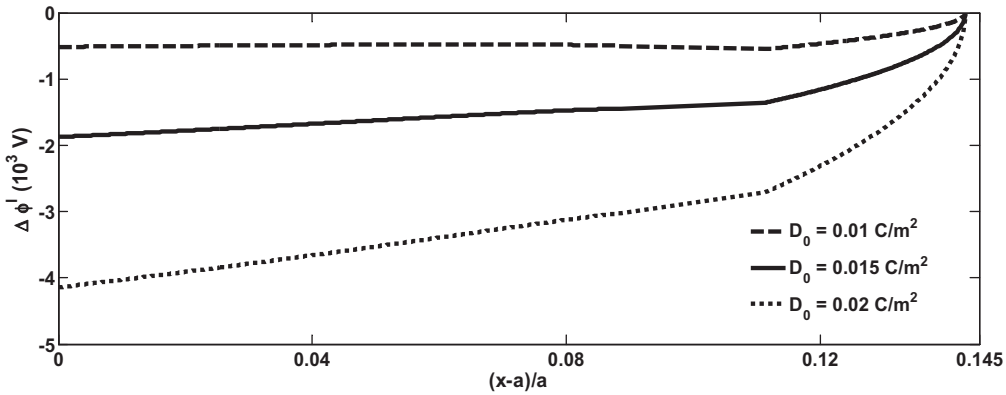

Fig. 2. Variation of COP over saturation zone with different D_0 for Case I.

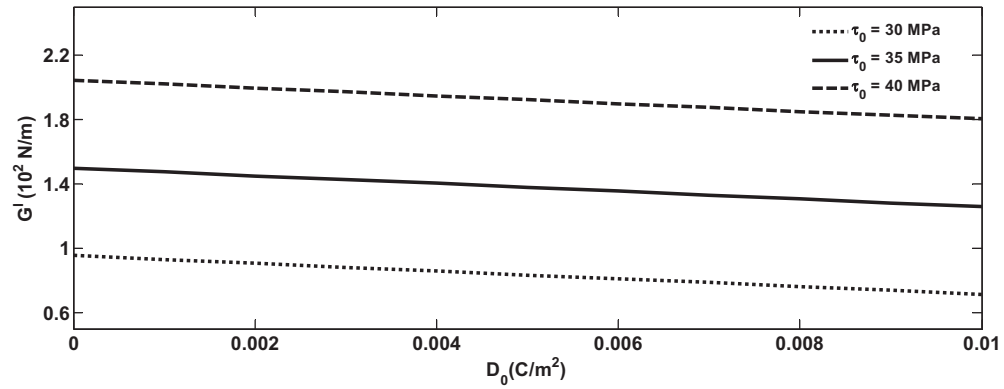

Fig. 3. ERR versus D_0 with different prescribed mechanical loading for Case I.

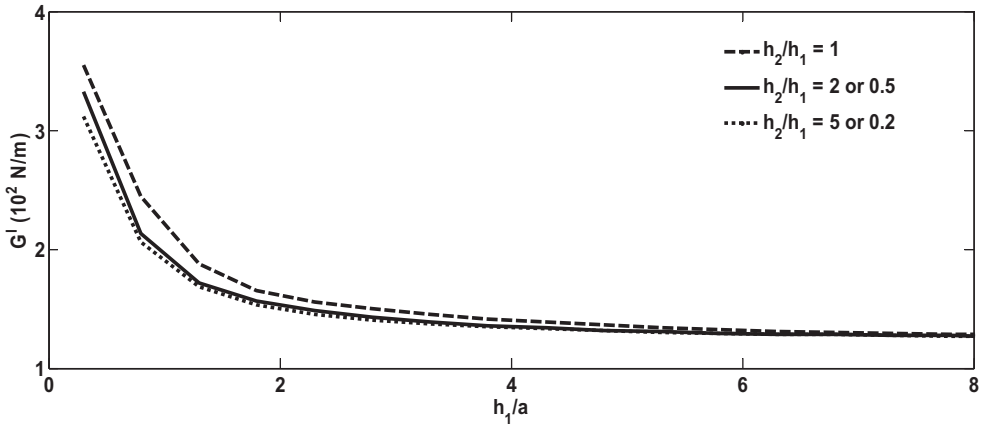

Fig. 4. Variation of ERR with respect to h_1/a for different h_2/h_1 for Case I.

$$\gamma_{zy}^{II} = \Psi_{,y}^{II} - (e_{15}/c_{44})\phi_{,y}^{II}, \tag{60}$$

$$E_y^{II} = -\phi_{,y}^{II}, \tag{61}$$

$$\text{where } \bar{\epsilon}_{11} = \epsilon_{11} + \frac{e_{15}^2}{c_{44}}, \tag{62}$$

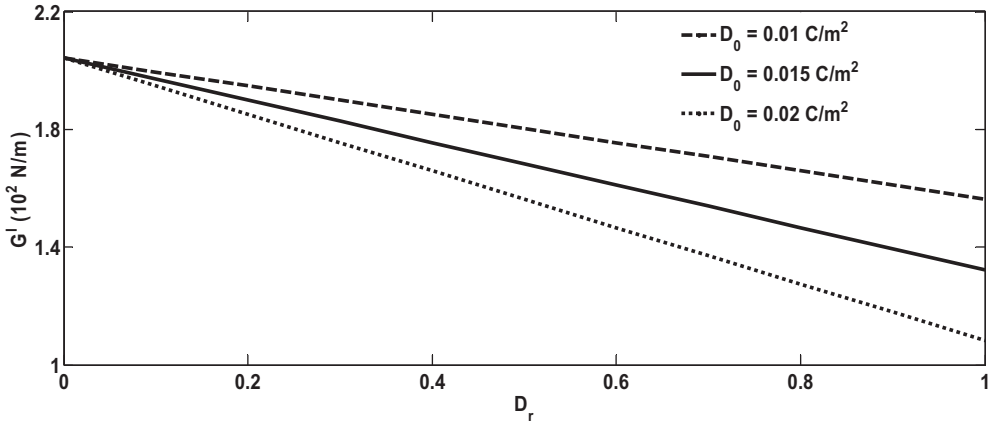

Fig. 5. Variation of ERR with respect to D_r for different D_0 for Case I.

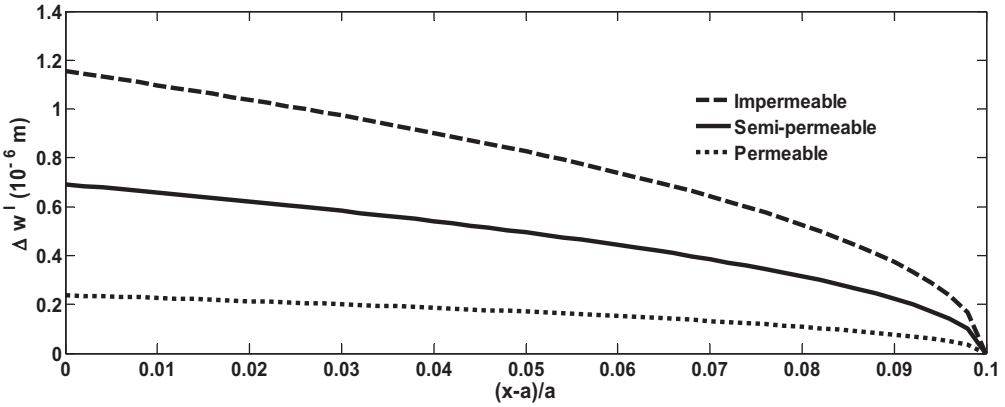

Fig. 6. CSD over the slide-yield zone with different crack-face electric boundary conditions for Case I.

and governing equations reduce to

$$\nabla^2\Psi^{II} = 0 \text{ and } \nabla^2\phi^{II} = 0. \tag{63}$$

General solution of Eqs. (63), analogous to Case I, may be written in the form

$$\Psi^{II}_{(i)}(x,y) = \int_0^\infty \left[A_{(i)}(\xi)\cosh(y\xi) + B_{(i)}(\xi)\sinh(y\xi)\right]\cos(x\xi)d\xi, \tag{64}$$

$$\phi^{II}_{(i)}(x,y) = \int_0^\infty \left[C_{(i)}(\xi)\cosh(y\xi) + F_{(i)}(\xi)\sinh(y\xi)\right]\cos(x\xi)d\xi, \tag{65}$$

where arbitrary functions $A_{(i)}(\xi)$, $B(\xi)$, $C_{(i)}(\xi)$ and $F_{(i)}(\xi)$ remain the same as in Case I,

With the aid of Eqs. (58)–(61) together Eqs. (64) and (65), the components of stress, electric displacement, strain and electric field are determined and written as

$$\sigma^{II}_{zy(i)}(x,y) = c_{44}\int_0^\infty \xi\left[A_{(i)}(\xi)\sinh(y\xi) + B_{(i)}(\xi)\cosh(y\xi)\right]\cos(x\xi)d\xi, \tag{66}$$

$$D^{II}_{y(i)}(x,y) = \int_0^\infty \xi\left[\{e_{15}A_{(i)}(\xi) - \bar{\epsilon}_{11}C_{(i)}(\xi)\}\sinh(y\xi) + \{B_{(i)}(\xi) - \bar{\epsilon}_{11}F_{(i)}(\xi)\}\cosh(y\xi)\right],\cos(x\xi)d\xi, \tag{67}$$

$$\gamma^{II}_{zy(i)}(x,y) = \int_0^\infty \xi\left[\{A_{(i)}(\xi) - (e_{15}/c_{44})C_{(i)}(\xi)\}\sinh(y\xi) + \{B_{(i)}(\xi) - (e_{15}/c_{44})F_{(i)}(\xi)\}\cosh(y\xi)\right]\cos(x\xi)d\xi, \tag{68}$$

$$E^{II}_{y(i)}(x,y) = -\int_0^\infty \xi\left[C_{(i)}(\xi)\sinh(y\xi) + F_{(i)}(\xi)\cosh(y\xi)\right]\cos(x\xi)d\xi. \tag{69}$$

Boundary conditions (iii) and (iv) substituting into Eqs. (57), (64)–(67) and simplifying, following two sets of dual integral equations are obtained

$$c_{44}\int_0^\infty \xi A_{(1)}(\xi)\tanh(h_1\xi)\cos(x\xi)d\xi = \tau_0 - \tau_s H(x-a), \quad 0 \leqslant x < b, \tag{70}$$

$$\int_0^\infty [1+M_{12}(\xi)]\{c_{44}A_{(1)}(\xi) - e_{15}C_{(1)}(\xi)\}\cos(x\xi)d\xi = 0, \quad b \leqslant x < \infty, \tag{71}$$

$$\int_0^\infty \xi\left[e_{15}A_{(1)}(\xi) - \bar{\epsilon}_{11}C_{(1)}(\xi)\right]\tanh(h_1\xi)\cos(x\xi)d\xi = -f_1 + D_s H(x-a), \quad 0 \leqslant x < c, \tag{72}$$

$$\int_0^\infty [1+M_{12}(\xi)]C_{(1)}(\xi)\cos(x\xi)d\xi = 0, \quad c \leqslant x < \infty. \tag{73}$$

For this case, we introduce $A_{(1)}(\xi)$ and $C_{(1)}(\xi)$ in term of new auxiliary functions $\Omega_1^{II}(.)$ and $\Omega_2^{II}(.)$, respectively, as

$$A_{(1)}(\xi) = \frac{2b^2}{[1+M_{12}(\xi)]}\int_{u=0}^1 \sqrt{u}\,\Omega_1^{II}(u)J_0(bu\xi)du, \tag{74}$$

$$C_{(1)}(\xi) = -\frac{2c^2}{[1+M_{12}(\xi)]}\int_{u=0}^1 \sqrt{u}\,\Omega_2^{II}(u)J_0(cu\xi)du. \tag{75}$$

Analogous to Case I, substituting Eqs. (74) and (75) into Eqs. (70)–(73), two Fredholms integral equations of second kind are obtained to determine $\Omega_1^{II}(.)$ and $\Omega_2^{II}(.)$, as

$$\Omega_1^{II}(x) + \int_{t=0}^1 K_1(x,t)\Omega_1^{II}(t)dt = \frac{\sqrt{x}}{c_{44}}\left[\tau_0 - \frac{2}{\pi}\tau_s\cos^{-1}\frac{a}{bx}\right], \tag{76}$$

$$\Omega_2^{II}(x) + \int_{t=0}^1 K_2(x,t)\Omega_2^{II}(t)dt = \frac{\sqrt{x}}{c_{44}\bar{\epsilon}_{11}}\left[f_4 - \frac{2}{\pi}f_5\cos^{-1}\frac{a}{cx}\right], \tag{77}$$

where $f_4 = c_{44}f_1 - e_{15}\tau_0$, $f_5 = c_{44}D_s - e_{15}\tau_s$.

6.1. Applications

Carrying the calculation analogous to Case I, stress intensity factor, K_{III}^{τ}, strain intensity factor, K_{III}^{γ}, electrical displacement factor, K_I^D, and electric-field intensity factor, K_I^E, for Case II are obtained as

$$K_{III}^{\tau} = c_{44}\sqrt{\pi b}\Omega_1^{II}(1), \tag{78}$$

$$K_{III}^{\gamma} = \sqrt{\pi b}\Omega_1^{II}(1), \tag{79}$$

$$K_I^D = \bar{\epsilon}_{11}\sqrt{\pi c}\Omega_2^{II}(1), \tag{80}$$

$$K_I^E = \sqrt{\pi c}\Omega_2^{II}(1). \tag{81}$$

The explicit expressions for slide-yield zone and saturation zone size may be obtained using Dugdale hypothesis as in Case I. The size of slide-yield zone is determined using $|b-a|$, where b may be determined from the following equation

$$\frac{b}{a} = \sec\left(\frac{\pi}{2}.\frac{\tau_0 - c_{44}R_3}{\tau_s}\right), \tag{82}$$

where $R_3 = \int_{t=0}^1 K_1(1,t)\Omega_1^{II}(t)dt$.

Similarly, the explicit expression for the saturation zone size is obtained as

$$\frac{c}{a} = \sec\left(\frac{\pi}{2}.\frac{f_4 - \bar{\epsilon}_{11}c_{44}R_4}{f_5}\right), \tag{83}$$

where $R_4 = \int_{t=0}^1 K_2(1,t)\Omega_2^{II}(t)dt$. The size of saturation zone is then determined using $|c-a|$.

Crack opening potential drop across the faces of saturation zone is obtained as

$$\Delta\phi^{II}(x) = \Phi_{(1)}^{II}(x,0^+) - \Phi_{(2)}^{II}(x,0^-) = 2\sqrt{c^2-x^2}\Omega_2^{II}(1), \quad a \leqslant x < c. \tag{84}$$

Similarly, crack sliding displacement across the slide-yield zone faces is given as

$$\Delta w^{II}(x) = w^{II}_{(1)}(x,0^+) - w^{II}_{(2)}(x,0^-) = 2\sqrt{b^2-x^2}\,\Omega^{II}_1(1) - (e_{15}/c_{44})\Delta\phi^{II}(x), \quad a \leqslant x < b. \tag{85}$$

The ECCP D_r for this case under permeable condition may be written as

$$(D_r)_{\text{perm}} = 1 - \frac{e_{15}\tau_0 + (2/\pi)f_5\cos^{-1}(a/c) + \bar{\epsilon}_{11}c_{44}R_4}{c_{44}D_0}. \tag{86}$$

For permeable crack, $D_r = (D_r)_{\text{perm}}$ and for semi-permeable crack $0 < D_r < (D_r)_{\text{perm}}$.
Energy release rate at the crack tip $x = a$, is calculated using formula

$$\begin{aligned} G^{II}_a &= \tau_s\Delta w^{II}(a) + D_s\Delta\phi^{II}(a), \\ &= \tau_s\left(2\sqrt{b^2-a^2}\,\Omega^{II}_1(1) - 2(e_{15}/c_{44})\sqrt{c^2-a^2}\,\Omega^{II}_2(1)\right) + 2D_s\sqrt{c^2-a^2}\,\Omega^{II}_2(1). \end{aligned} \tag{87}$$

6.2. Numerical case study for Case II

Case study similar to Case I is carried for Case II as well.

Fig. 7 depicts the variation of COP over the saturation zone for a non-centric semi-permeable cut in $BaTiO_3$ piezoelectric strip. Magnitude of COP decreases parabolically and becomes zero at saturation zone tip, as expected. Also the effect of prescribed electric-displacement (D_0) on COP shows that a slight increase in electric displacement (D_0 from 0.01 to 0.02 C/m^2) increases the magnitude of COP (although in negative sense).

Fig. 8 shows the variation of ERR versus applied electric displacement (D_0) for various values of prescribed mechanical load (τ_0). It is noted that ERR decreases linearly continuously with increasing the value of D_0. It shows that electric load retards the crack opening for this case too. However increasing the mechanical loads, the ERR increases but the decreasing trends with respect to D_0 of ERR continues, affirming the crack arrest. It is also pointed that ERR for this case is high as compare to the ERR for Case I.

Fig. 9 depicts ERR variation with respect to h_1/a for different h_2/h_1 ratio. It is seen that ERR is higher when the crack is situated on the center line of the strip and when the crack is situated off center line of the strip, the ERR is less with continues decreasing trend.

The effect of electric displacement on ERR versus electric crack condition parameter is plotted in the Fig. 10. It is observed that trend of ERR with respect to ECCP is same as in Case I and ERR is higher in impermeable case, $D_r = 0$, as compare to Case I.

The effect of semi-permeable crack-face boundary conditions on CSD versus normalized slide-yield zone is shown in Fig. 11. It is observed that behavior of CSD with respect to slide-yield zone and electric boundary conditions over the crack-faces is same as in Case I. From the figure, one interesting point is observed that the electric crack-face boundary condition is effecting CSD up to saturation zone tip $\{(x-a)/a \approx 0.1\}$. And beyond this point, the effect of crack media on CSD is negligible.

6.3. Validation of obtained results for Case II

Our results validate with those of Shen et al. [12] by putting $h_1 = h_2 \to \infty$ and $D_r = 0$.

7. Case III: when saturation and slide-yield zones are of equal length ($b = c$)

For mathematical convenience, two potentials functions $\Psi^{III}(x,y)$ and $\Phi^{III}(x,y)$ are introduced as

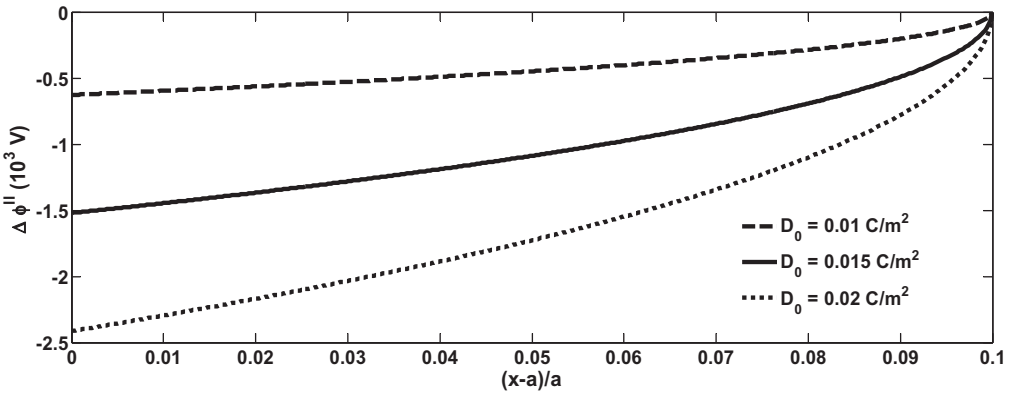

Fig. 7. COP profile over saturation zone with different prescribed D_0 for Case II.

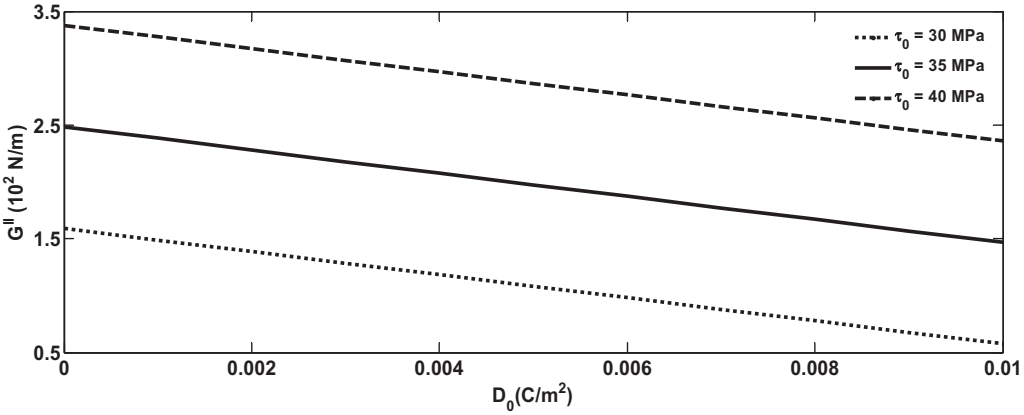

Fig. 8. Effect of τ_0 for non-centric crack on ERR with variation in D_0 for Case II.

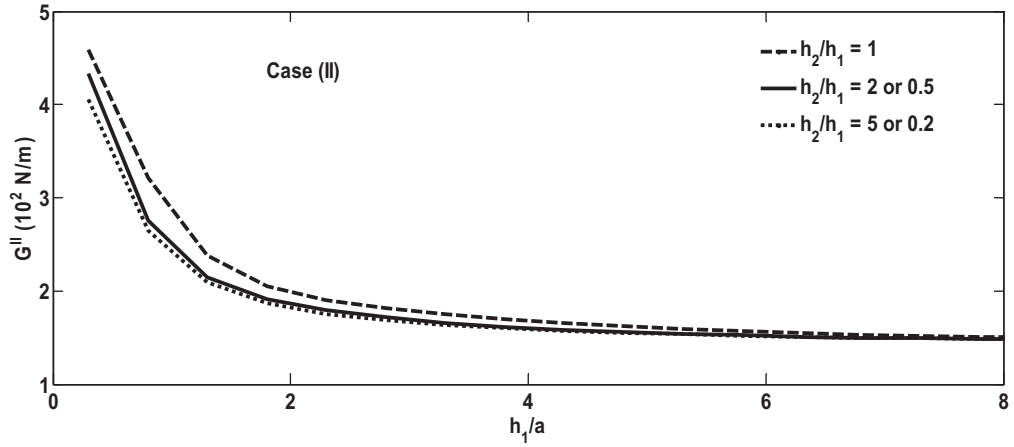

Fig. 9. Variation in ERR with respect to h_1/a for different width ratio of strip for Case II.

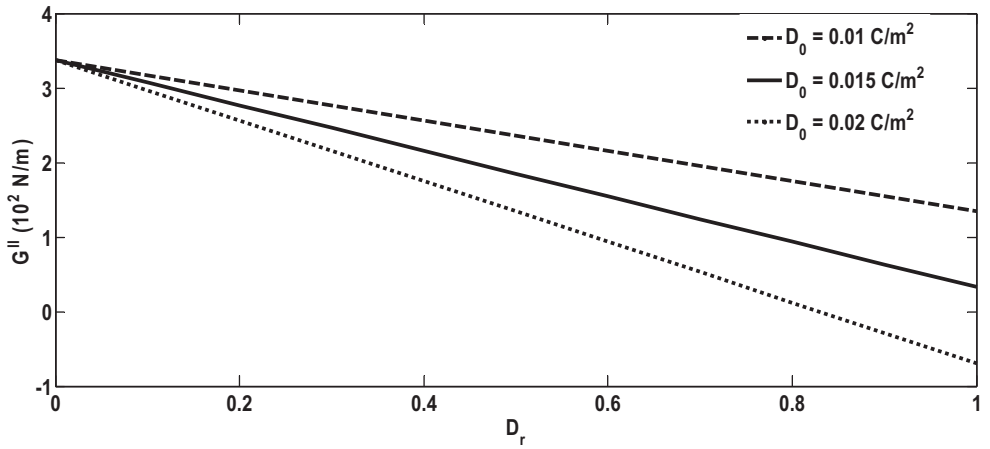

Fig. 10. Variation of ERR with respect to D_r for different D_0 for Case II.

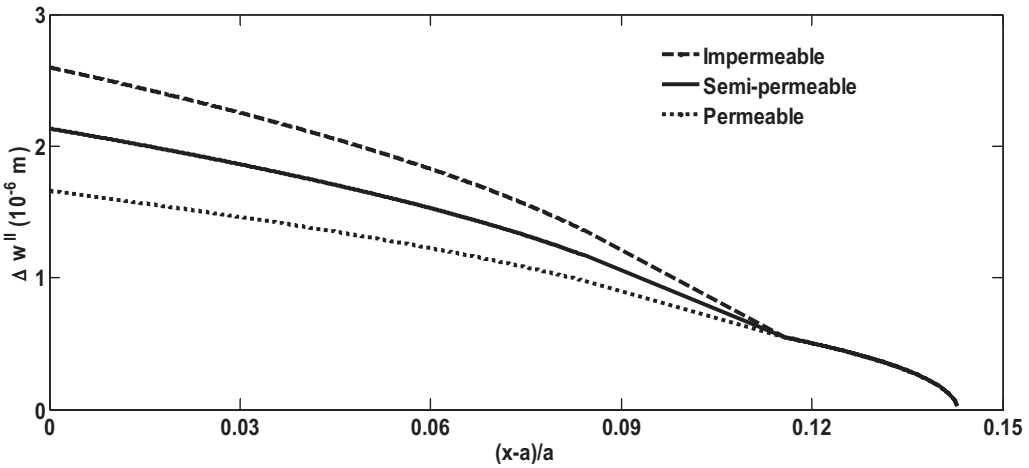

Fig. 11. CSD profile over slide-yield zone with different crack medium for Case II.

$$\Psi^{III}(x,y) = w^{III}(x,y) + (e_{15}/c_{44})\phi^{III}(x,y), \tag{88}$$

$$\Phi^{III}(x,y) = \phi^{III}(x,y) - (e_{15}/\epsilon_{11})w^{III}(x,y). \tag{89}$$

With the help of Eqs. (88) and (89), the Eqs. (3)–(8) reduce to

$$\sigma_{zy}^{III} = c_{44}\Psi_{,y}^{III}, \tag{90}$$

$$D_{y}^{III} = -\epsilon_{11}\Phi_{,y}^{III}, \tag{91}$$

$$\gamma_{zy}^{III} = (1/\bar{c}_{44})\left[c_{44}\Psi_{,y}^{III} - e_{15}\Phi_{,y}^{III}\right], \tag{92}$$

$$E_{y}^{III} = (1/\bar{\epsilon}_{11})\left[e_{15}\Psi_{,y}^{III} + \epsilon_{11}\Phi_{,y}^{III}\right], \tag{93}$$

and

$$\nabla^2\Psi^{III}(x,y) = 0 \text{ and } \nabla^2\Phi^{III}(x,y) = 0. \tag{94}$$

Superscript III denotes that the quantities refer to Case III.
General solution of Laplace Eq. (94) may be written as

$$\Psi_{(i)}^{III}(x,y) = \int_0^\infty \left[A_{(i)}(\xi)\cosh(y\xi) + B_{(i)}(\xi)\sinh(y\xi)\right]\cos(x\xi)d\xi, \tag{95}$$

$$\Phi_{(i)}^{III}(x,y) = \int_0^\infty \left[C_{(i)}(\xi)\cosh(y\xi) + F_{(i)}(\xi)\sinh(y\xi)\right]\cos(x\xi)d\xi. \tag{96}$$

Substituting Eqs. (95) and (96) into Eqs. (90)–(93), one obtains desired components of stress, electric displacement, strain, electric field as

$$\sigma_{zy(i)}^{III}(x,y) = c_{44}\int_0^\infty \xi\left[A_{(i)}(\xi)\sinh(y\xi) + B_{(i)}(\xi)\cosh(y\xi)\right]\cos(x\xi)d\xi, \tag{97}$$

$$D_{y(i)}^{III}(x,y) = -\epsilon_{11}\int_0^\infty \xi\left[C_{(i)}(\xi)\sinh(y\xi) + F_{(i)}(\xi)\cosh(y\xi)\right]\cos(x\xi)d\xi, \tag{98}$$

$$\gamma_{zy(i)}^{III}(x,y) = (1/\bar{c}_{44})\int_0^\infty \xi[c_{44}A_{(i)}(\xi) - e_{15}C_{(i)}(\xi)\}\sinh(y\xi) + \{c_{44}B_{(i)}(\xi) - e_{15}F_{(i)}(\xi)\}\cosh(y\xi)]\cos(x\xi)d\xi, \tag{99}$$

$$E_{y(i)}^{III}(x,y) = (1/\bar{\epsilon}_{11})\int_0^\infty \xi[\{e_{15}A_{(i)}(\xi) + \epsilon_{11}C_{(i)}(\xi)\}\sinh(y\xi) + \{e_{15}B_{(i)}(\xi) + \epsilon_{11}F_{(i)}(\xi)\}\cosh(y\xi)]\cos(x\xi)d\xi. \tag{100}$$

As in the previous cases, with analogous calculation following two sets of dual integral equations are obtained

$$c_{44}\int_0^\infty \xi A_{(1)}(\xi)\tanh(h_1\xi)\cos(x\xi)d\xi = \tau_0 - \tau_s H(x-a), \quad 0 \leqslant x < b, \tag{101}$$

$$\int_0^\infty [1+M_{12}(\xi)]\{c_{44}A_{(1)}(\xi) - e_{15}C_{(1)}(\xi)\}\cos(x\xi)d\xi = 0, \quad b \leqslant x < \infty, \tag{102}$$

$$\epsilon_{11}\int_0^\infty \xi C_{(1)}(\xi)\tanh(h_1\xi)\cos(x\xi)d\xi = -f_1 + D_s H(x-a), \quad 0 \leqslant x < b, \tag{103}$$

$$\int_0^\infty [1+M_{12}(\xi)]\{e_{15}A_{(1)}(\xi) + \epsilon_{11}C_{(1)}(\xi)\}\cos(x\xi)d\xi = 0, \quad b \leqslant x < \infty. \tag{104}$$

Introducing $A_{(1)}(\xi)$ and $C_{(1)}(\xi)$ for this case as

$$A_{(1)}(\xi) = \frac{2b^2}{[1+M_{12}(\xi)]}\int_{u=0}^1 \sqrt{u}\,\Omega_1^{III}(u)J_0(bu\xi)du, \tag{105}$$

$$C_{(1)}(\xi) = -\frac{2b^2}{[1+M_{12}(\xi)]}\int_{u=0}^1 \sqrt{u}\,\Omega_2^{III}(u)J_0(bu\xi)du. \tag{106}$$

Substituting these values into Eqs. (101)–(104), one obtains following Fredholm integral equation of second kind to determine $\Omega_1^{III}(\cdot)$ and $\Omega_2^{III}(\cdot)$ as

$$\Omega_1^{III}(x) + \int_{t=0}^1 K_1(x,t)\Omega_1^{III}(t)dt = \frac{\sqrt{x}}{c_{44}}\left[\tau_0 - \frac{2}{\pi}\tau_s\cos^{-1}\frac{a}{bx}\right], \tag{107}$$

$$\Omega_2^{III}(x) + \int_{t=0}^1 K_2(x,t)\Omega_2^{III}(t)dt = \frac{\sqrt{x}}{\epsilon_{11}}\left[f_1 - \frac{2}{\pi}D_s\cos^{-1}\frac{a}{bx}\right], \tag{108}$$

where $K_1(x,t)$ and $K_2(x,t)$ are kernels and defined as

$$K_1(x,t) = K_2(x,t) = \sqrt{xt}\int_{y=0}^\infty y\{\chi(y/b)-1\}J_0(xy)J_0(ty)dy. \tag{109}$$

7.1. Applications for Case III

Similar to the Case I and Case II, we calculate mode-III stress and strain intensity factors at the tip $x = b$ as

$$K_{III}^{\tau} = \lim_{x\to b^+}\left\{\sqrt{2\pi(x-b)}\sigma_{zy(1)}^{III}(x,0^+)\right\} = c_{44}\sqrt{\pi\, b}\,\Omega_1^{III}(1), \tag{110}$$

$$K_{III}^{\gamma} = \lim_{x\to b^+}\left\{\sqrt{2\pi(x-b)}\gamma_{zy(1)}^{III}(x,0^+)\right\} = \sqrt{\pi b}\,\Omega_1^{III}(1). \tag{111}$$

And mode-I electric-displacement and electric field intensity factors at the tip of saturation zone are obtained as

$$K_I^D = \lim_{x\to b^+}\left\{\sqrt{2\pi(x-b)}D_{y(1)}^{III}(x,0^+)\right\} = \epsilon_{11}\sqrt{\pi b}\,\Omega_2^{III}(1), \tag{112}$$

$$K_I^E = \lim_{x\to b^+}\left\{\sqrt{2\pi(x-b)}E_{y(1)}^{III}(x,0^+)\right\} = \sqrt{\pi b}\,\Omega_2^{III}(1). \tag{113}$$

Length of developed slide-yield zone and saturation zone may be calculated from the following expressions

$$\frac{b}{a} = \sec\left(\frac{\pi}{2}.\frac{\tau_0 - c_{44}R_5}{\tau_s}\right), \tag{114}$$

and

$$\frac{b}{a} = \sec\left(\frac{\pi}{2}.\frac{f_1 - \epsilon_{11}R_6}{D_s}\right), \tag{115}$$

respectively, where $R_5 = \int_{t=0}^1 K_1(1,t)\Omega_1^{III}(t)dt$ and $R_6 = \int_{t=0}^1 K_2(1,t)\Omega_2^{III}(t)dt$.

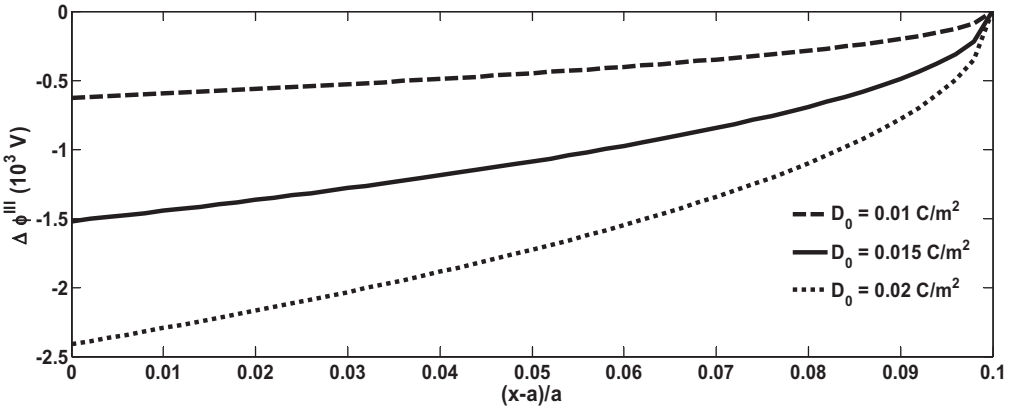

Fig. 12. Variation in COP over normalized saturation zone with D_0 for Case III.

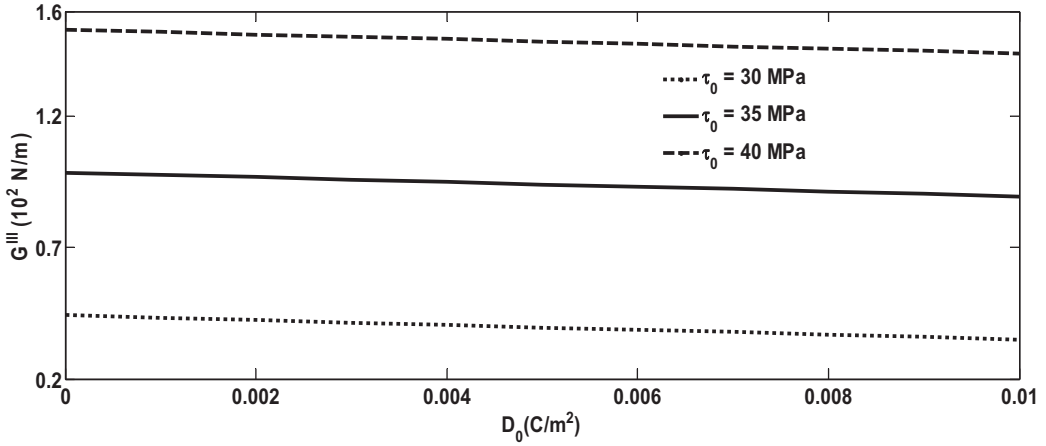

Fig. 13. Effect of τ_0 for non-centric crack on ERR with variation in D_0 for Case III.

Crack opening potential drop and crack sliding displacement for this case across the saturation and slide-yield zones are written as

$$\Delta\phi^{III}(x) = \Phi^{III}_{(1)}(x,0^+) - \Phi^{III}_{(2)}(x,0^-) = \frac{2\sqrt{b^2-x^2}}{\bar{\epsilon}_{11}}\left[e_{15}\Omega^{III}_1(1) - \epsilon_{11}\Omega^{III}_2(1)\right], \quad 0 < x \leqslant b, \tag{116}$$

$$\Delta w^{III}(x) = w^{III}_{(1)}(x,0^+) - w^{III}_{(2)}(x,0^-) = \frac{2\sqrt{b^2-x^2}}{\bar{c}_{44}}\left[c_{44}\Omega^{III}_1(1) + e_{15}\Omega^{III}_2(1)\right], \quad 0 < x \leqslant b, \tag{117}$$

and

$$(D_r)_{\text{perm}} = 1 - \frac{e_{15}\tau_0 - (2/\pi)[e_{15}\tau_s + c_{44}D_s]\cos^{-1}(a/b) - e_{15}c_{44}R_5 + c_{44}\epsilon_{11}R_6}{c_{44}D_0}. \tag{118}$$

Energy release rate at the crack tip, $x = a$, using Eqs. (116) and (117) may be written as

$$G^{III}_a = \tau_s\Delta w^{III}(a) + D_s\Delta\phi^{III}(a), = 2\sqrt{b^2-a^2}\left[\left(\frac{c_{44}}{\bar{c}_{44}}\tau_s + \frac{e_{15}}{\bar{\epsilon}_{11}}D_s\right)\Omega^{III}_1(1) + \left(\frac{e_{15}}{\bar{c}_{44}}\tau_s - \frac{\epsilon_{11}}{\bar{\epsilon}_{11}}D_s\right)\Omega^{III}_2(1)\right]. \tag{119}$$

7.2. Illustrative study for Case III

For this case, a case study is presented for cracked $BaTiO_3$ piezoelectric strip under out-of-plane mechanical loading $\tau_0 = 40$ MPa and in-plane electric displacement $D_0 = 0.02$ C/m^2.

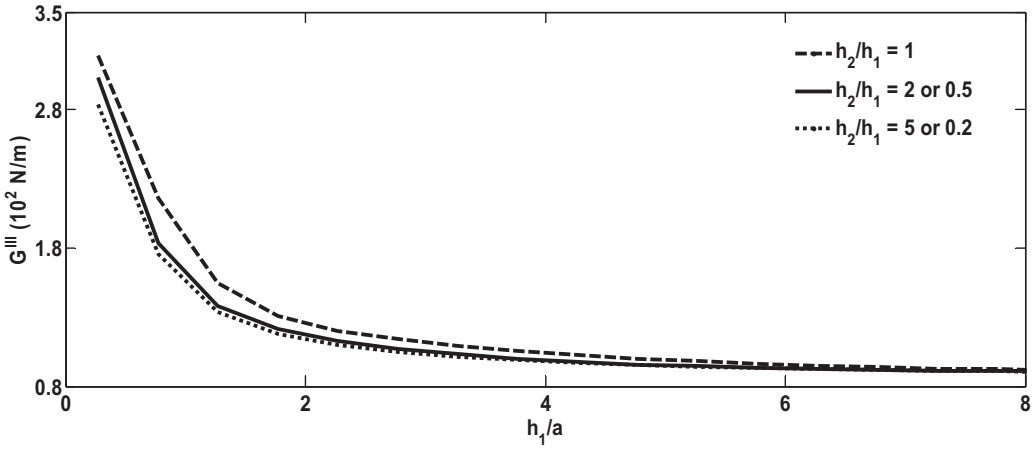

Fig. 14. Variation of ERR with respect to h_1/a for different h_2/h_1 for Case III.

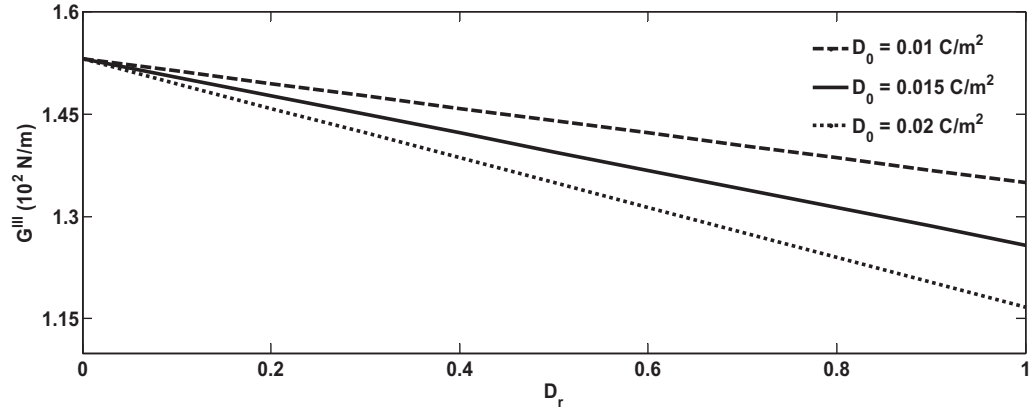

Fig. 15. Variation of ERR with respect to D_r for different D_0 for Case III.

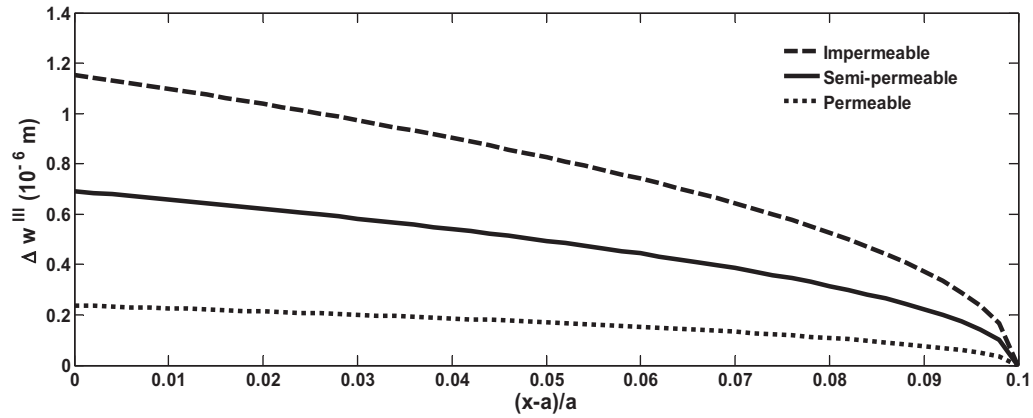

Fig. 16. CSD versus slide-yield zone with different crack medium for Case III.

Variation in COP over the developed slide-yield/saturation zones is depicted in Fig. 12. From the figure, it is observed that COP profile shows a similar variation as in Cases I and II. Since both zones are equal so no kink point is observed on the graphs of COP.

The effect of combined electromechanical loadings on energy release rate is drawn in Fig. 13. From the figure, it is observed that ERR linearly decreases with increase in D_0. And as the prescribed mechanical loads are increased the ERR also increases although the decreasing trends continue with respect to D_0.

ERR versus h_1/a ratio is plotted in Fig. 14. The variation is same as in Cases I and II with width ratio with a difference that the ERR starts with lower values.

Variation of ERR versus ECCP for different electric displacement is plotted in the Fig. 15. The behavior is same as in Case I and Case II with ECCP and D_0 with a difference that the ERR starts with lower values for impermeable case as compare to Case I and Case II.

Fig. 16 depicts the behavior of CSD over the slide-yield zone for impermeable, semi-permeable and permeable crack. The behavior of CSD over the slide-yield zone is similar as in Case I and Case II. From Figs. 6, 11 and 16, it is observed that CSD is maximum for Case II and minimum for Case III, while for semi-permeable case it lies in between.

7.3. Validation of results for Case III

For this case also the results match with those of Shen et al. [12] by putting $b = c$, also $D_r = 0$, $h_1 \to \infty$ and $h_2 \to \infty$.

8. Conclusions

- An electrical and mechanical yielding model is proposed for semi-permeable non-centric crack and solved using Fourier integral transform technique. The cases considered are: when saturation zone is bigger, smaller and equal to slide-yield zone.
- A comparison between ERR for Cases I, II and III concludes that crack opens more for case when slide-yield zone is bigger than saturation zone followed by saturation zone bigger than slide-yield zone. And it will be minimum when both saturation and slide-yield zones are equal. It is also noted that ERR is low for non-symmetrically located crack vis-à-vis centrically located crack.
- It is noted that the crack-sliding displacement strongly depends on crack-face boundary conditions. As the permittivity of the medium inside the crack increases the relative crack sliding decreases.
- Energy release rate also depends on permittivity of the crack media. As permittivity of the crack media increases the ERR decreases, indicates the less crack growth for high value of ECCP.
- Finally, numerical case study affirms that considered crack model is capable to crack arrest for non-centric case semi-permeable crack conditions under small-scale mechanical yielding and electric yielding.

Acknowledgements

The authors are grateful to Prof. R.D. Bhargava {Sr. Prof. and Head (retd.), Department of Mathematics, Indian Institute of Technology Bombay, Mumbai} for continuous encouragement during course of this work. The second author is thankful to MHRD for the financial support.

References

[1] T.H. Hao, Z.Y. Shen, A new electric boundary condition of electric fracture mechanics and its applications, Eng. Fract. Mech. 47 (1994) 793–802.
[2] Z.-G. Zhou, L.-Z. Wu, S.-Y. Du, Non-local theory solution for a Mode I crack in piezoelectric materials, Eur. J. Mech. A/Solids 25 (2006) 793–807.
[3] C. Boldrini, E. Viola, Crack energy density of a piezoelectric material under general electromechanical loading, Theoret. Appl. Fract. Mech. 49 (2008) 321–333.
[4] Q. Li, Y. Chen, Investigation of the crack problem in non-local piezoelectric materials under combined electromechanical loadings, Acta. Mech. Sin. 25 (2009) 219–225.
[5] B.L. Wang, J.-C. Han, Effect of finite cracking on the electromechanical coupling properties of piezoelectric materials, Int. J. Fract. 164 (2010) 201–212.
[6] H. Gao, T.Y. Zhang, P. Tong, Local and global energy release rates for an electrically yield crack in piezoelectric ceramics, J. Mech. Phys. Solids 45 (1997) 491–510.
[7] D.S. Dugdale, Yielding of steel sheets containing slits, J. Mech. Phys. Solids 8 (1960) 100–104.
[8] T.C. Wang, Analysis of strip electric saturation model of crack problem in piezoelectric materials, Int. J. Solids Struct. 37 (2000) 6031–6049.
[9] S. Li, On saturation-strip model of a permeable crack in a piezoelectric ceramic, Acta Mech. 165 (2003) 47–71.
[10] F. Narita, Y. Shindo, Fatigue crack propagation in a piezoelectric ceramic strip subjected to mode III loading, Acta Mech. 137 (1999) 55–63.
[11] F. Narita, Y. Shindo, Mode I crack growth rate for yield strip model of a narrow piezoelectric ceramic body, Theor. Appl. Fract. Mech. 36 (2001) 73–85.
[12] S. Shen, T. Nishioka, Z.B. Kuang, Z. Liu, Nonlinear electromechanical interfacial fracture for piezoelectric materials, Mech. Mater. 32 (2000) 57–64.
[13] R.R. Bhargava, A. Setia, Crack arrest saturation model under combined electrical and mechanical loadings, J. Achieve Mater. Manuf. Eng. 37 (2009) 544–548.
[14] C.Q. Ru, X. Mao, Conducting cracks in a piezoelectric ceramic of limited electrical polarization, J. Mech. Phys. Solids 47 (1999) 2125–2146.
[15] V. Loboda, Y. Lapusta, A. Sheveleva, Analysis of pre-fracture zones for electrically permeable crack in an interlayer piezoelectric material, Int. J. Fract. 140 (2006) 307–313.
[16] X.C. Zhong, K.S. Zhang, Electroelastic analysis of an electrically dielectric Griffith crack in piezoelectric layer, Int. J. Eng. Sci. 48 (2010) 612–623.
[17] S.M. Kwon, Electrical nonlinear anti-plane shear crack in a functionally graded piezoelectric strip, Int. J. Solids Struct. 40 (2003) 5649–5667.
[18] I.M. Ryzhik, I.S. Gradshteyn, Table of Integrals, Series and Products, Academic Press, New York, 1965.
[19] Z.C. Ou, X. Wu, On the crack-tip stress singularity of interfacial cracks in transversely isotropic piezoelectric bi-materials, Int. J. Solids Struct. 40 (2003) 7499–7511.